A&A 466, 823–830 (2007)
DOI: 10.1051/0004-6361:20065096

Astronomy & Astrophysics

Chandra and Spitzer observations of CDFS X-ray obscured QSOs⋆

I. Georgantopoulos[1], A. Georgakakis[2], and A. Akylas[1]

[1] Institute of Astronomy & Astrophysics, National Observatory of Athens, Palaia Penteli, 15236, Athens, Greece
[2] Astrophysics Group, Blackett Laboratory, Imperial College, Prince Consort Road, SW7 2BZ, UK

Received 27 February 2006 / Accepted 28 October 2006

ABSTRACT

We present *Chandra* and *Spitzer* data for the 186, extragalactic, hard 2–10 keV X-ray selected sources, which lie in the central part of the Chandra Deep Field South (CDFS). For the vast majority of sources (99.5%), there is a spectroscopic or photometric redshift available. We classify 17 sources as X-ray obscured QSOs, strictly according to X-ray criteria, i.e. defined as having large hydrogen column densities ($N_{\rm H} > 10^{22}$ cm^{-2}) and luminosities ($L_{\rm x} > 10^{44}$ erg s^{-1}). The surface density of X-ray obscured QSOs is ∼210 deg^{-2}. We find 18 candidate Compton-thick $N_{\rm H} > 10^{24}$ cm^{-2} sources, of which three have QSO luminosities ($L_{\rm x} > 10^{44}$ erg s^{-1}). The X-ray obscured QSO comprise a mixed bag of objects, covering the redshift range $z = 1.3-4.3$. Eight of these show narrow-line optical spectra, two show no obscuration in their optical spectra that present broad lines, while for the other seven there is only a photometric redshift available. About half of the X-ray obscured QSOs show high X-ray to optical flux ratios, X/O > 1, and red colours, $I - 3.6\,\mu$m > 4. Combining the X-ray with the mid-IR 8 μm or 24 μm flux can be used as an additional diagnostic to sift out the heavily obscured AGN. All X-ray selected QSOs present red mid-IR colours and can be easily separated among mid-IR sources, demonstrating that mid-IR selection provides a powerful tool for detecting obscured QSOs.

Key words. galaxies: active – galaxies: quasars: general – X-rays: galaxies – X-rays: general

1. Introduction

Deep *Chandra* surveys have resolved a substantial fraction of the X-ray background in the 2–10 keV band (Brandt & Hasinger 2005). The vast majority of the detected sources in these fields are AGN, both unobscured ($N_{\rm H} < 10^{22}$ cm^{-2}) and obscured ($N_{\rm H} > 10^{22}$ cm^{-2}), with the latter dominating at faint fluxes. For example, at the source detection limit of the Chandra Deep Field South (CDF-S), $f_{\rm X}(2-10\,{\rm keV}) \sim 2\times10^{-16}$ erg s^{-1} cm^{-2}, about 80% of the sources have $N_{\rm H} > 10^{22}$ cm^{-2} (e.g. Alexander et al. 2003; Akylas et al. 2006).

However, there is clearly a scarcity of NL QSO. Steffen et al. (2003) find that the number of narrow line (NL) AGN decreases at bright luminosities and high redshift. Only a limited number of X-ray selected NL QSO ($L_{\rm X} > 10^{44}$ erg s^{-1}) have been identified at high-z (e.g. Stern et al. 2002; Norman et al. 2002).

These NL QSOs could be rare just because of selection effects (e.g. Treister et al. 2004). For example, rest-frame hard X-ray photons at high redshift can penetrate large obscuring columns but the observed optical emission, probing the rest-frame UV, will be easily diminished by even a small amount of dust. These sources will therefore be optically faint, hampering detailed analysis, and may be overlooked in follow-up studies. These sources however, are expected to have a high X-ray to optical flux ratio ($\log(f_{\rm x}/f_{\rm o}) > 1$ or X/O) or very red optical/near-IR colours. Fiore et al. (2003) indeed find that a fraction of the high X/O sources in the HELLAS2XMM survey are associated with NL AGN, in agreement with the above scenario. Similarly, Brusa et al. (2005) find that a significant fraction of obscured X-ray sources are associated with extremely red objects, ERO, defined as having $R - K > 5$, again supporting the idea that optical selection effects may play an important role.

Alternatively, the scarcity of NL QSOs may suggest that the AGN unification model does not hold well at high luminosities. It has been recently found that the fraction of X-ray obscured AGN decreases with increasing luminosity (Ueda et al. 2003; La Franca et al. 2005; Akylas et al. 2006). The physical interpretation could be that the highly luminous AGN blow the obscuring screen away or that they photoionize the surrounding gas.

To test the two different interpretations above, it is important to constrain the surface density of X-ray obscured QSOs (defined here as X-ray luminous, obscured sources) and to determine their properties. For instance, do X-ray obscured QSOs have high X/O ratios? Can they be selected through their red (e.g. $R - K$) colours? Do they all have NL or does a fraction present BL optical spectra (e.g. Akylas et al. 2004).

Padovani et al. (2004) searched for X-ray obscured QSOs in the CDF-N and CDF-S surveys using a high-luminosity and a hardness-ratio criterion, finding a few tens candidate X-ray obscured QSOs. However, a number of the X-ray obscured QSO redshifts and luminosities come indirectly from the empirical X/O correlation with X-ray luminosity (Fiore et al. 2003; Barger et al. 2003). Here, we attempt to study the properties of X-ray obscured QSOs in the hard X-ray selected (2–10 keV) CDF-S sample. A big advantage of this sample is that, for the vast majority of the sources (except one out of 247), there is either a spectroscopic or a photometric redshift available. This means that optical selection effects have little impact on our study. Moreover, we determine the X-ray spectral properties of the sources using spectral fittings instead of the crude and indirect method of hardness ratios, minimizing any uncertainties

⋆ Table 3 is only available in electronic form at
http://www.aanda.org

in the determination of the X-ray absorbing column density. Additionally, the wealth of data that has been recently accumulated in the CDFS region as part of the GOODS survey (e.g. Hubble ACS, *Spitzer*, Very Large Telescope photometry and spectroscopy) allows us to study the properties of the X-ray obscured QSOs in detail.

We use $H_0 = 75$ km s^{-1} Mpc^{-1}, $\Omega_{\rm m} = 0.3, \Omega_\Lambda = 0.7$ throughout the paper.

2. The data

2.1. X-ray data

The 1Ms CDFS data consist of 11 individual *Chandra* (Advanced CCD Imaging Spectrometer) ACIS-I pointings with the aim points separated by a few arcseconds. The aim point coordinates are $\alpha = 3^{\rm h}32^{\rm m}28\overset{\rm s}{.}0, \delta = -27°48'30''$ (J2000). More details are presented in Rosati et al. (2002) and Giacconi et al. (2002). The 247 sources were detected in the 2–10 keV band down to a flux limit of 2×10^{-16} erg cm^{-2} s^{-1} ($\Gamma = 1.4$). As the roll angles of the individual pointings were different, a fraction of the sources at the edge of the field-of-view are detected only in a smaller number of pointings. We choose here to analyse only the sources that lie in all 11 pointings, in order to maximise the photon statistics. Our source selection is such that the central field-of-view is covered. The 188 sources were detected within all 11 pointings covering an area of ∼0.05 deg^2. Two sources are associated with stars (Szokoly et al. 2004). Only one source has not been optically identified and thus there is no redshift (photometric or spectroscopic) available.

We used the *PSEXTRACT* script in the *CIAO* v3.2 software package to extract spectra. There are 30 sources with more than approximately 500 counts. The data were grouped so that there are 20 counts per bin for these sources and thus χ^2 statistics can apply. For the other sources with more limited photon statistics, we used the C-statistic technique (Cash 1979) specifically developed to extract spectral information from data with a low signal-to-noise ratio. We used the *XSPEC* v11.2 software package for the spectral fits. We fit the data using a power-law model absorbed by two cold absorbers: wa*wa*po in *XSPEC* notation. The first column was fixed to the Galactic (8×10^{19} cm^{-2}) while the second one is the observer's frame *intrinsic* column density. Then the rest-frame column density scales as $(1+z)^{2.7}$ (e.g. Barger et al. 2003). In the case of the sources with limited photon statistics (<500 counts), the power-law photon index was fixed to $\Gamma = 1.8$. The intrinsic luminosities were estimated using a K-correction appropriate for the best value of Γ. The X-ray spectral fits are presented in Table 3. The distribution of the rest-frame column density is shown in Fig. 1. All candidate Compton-thick sources are plotted in the last $N_{\rm H}$ bin.

2.2. Optical and mid-IR

Part of the CDFS was observed with the Advanced Camera Surveys (ACS) onboard the *Hubble* Space Telescope as part of the GOODS survey (Giavalisco et al. 2004). We use here the *F775W* filter data (roughly equivalent to the *I* band). We cross-correlate the X-ray sources with the ACS data using a radius of 3 arcsec. As the surface density of sources increases at faint magnitudes reaching $\sim 10^5$ deg^{-2} 0.5 mag^{-1} at $I = 26$ (Kashikawa et al. 2004) one has to be cautious about the possibility of a chance coincidence in the faintest cases (e.g. CDFS-610). For the sources that do not have *I*-band photometry available, we quote *R* magnitudes from Giacconi et al. (2002).

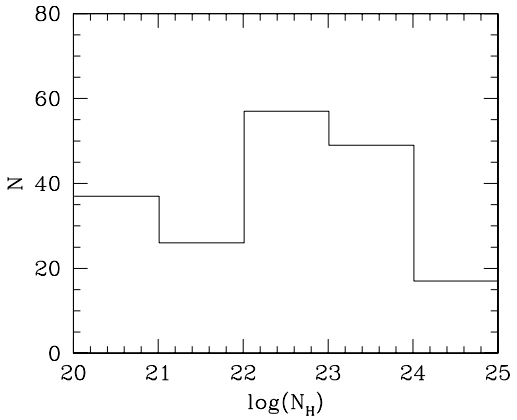

Fig. 1. The distribution of the rest-frame column density for all sources.

Part of the CDFS was observed by the IR *Spitzer* mission (Werner et al. 2004). The 8 μm and 24 μm fluxes were derived from the *Spitzer* Infrared Array Camera, IRAC, (Fazio et al. 2004) and Multiband Imaging Photometer, MIPS, (Rieke et al. 2004) flux calibrated, background subtracted images provided in the *Spitzer* archive[1]. We cross-correlated the *Spitzer* with the *Chandra* sources, again using a radius of 3 arcsec.

3. Results

3.1. The X-ray obscured QSOs

23 sources are defined as QSOs based on their high intrinsic luminosity ($L_{\rm x} > 10^{44}$ erg s^{-1}). Of these 18 (see Table 1) present high absorbing column densities ($N_{\rm H} > 10^{22}$ cm^{-2}) and are thus classified as absorbed QSOs (or X-ray obscured QSOs) purely on the basis of their X-ray spectrum and luminosity. However, at least one source (a BL QSO) is a borderline X-ray obscured QSO, as its column density uncertainty is relatively large. Source CDFS-24, which has a BL optical spectrum, is consistent with $N_{\rm H} = 0$ cm^{-2} at the 90% confidence level. We caution that a small error in the measured column density in the observer's frame (owing e.g. to a background fluctuation) may translate in an erroneously high column density at the high redshifts probed here (see Akylas et al. 2006). For example, as the rest-frame column density scales as $(1+z)^{2.7}$, a column as low as $\sim 2.5 \times 10^{20}$ in the observer's frame will pass the 10^{22} cm^{-2} rest-frame column threshold at a redshift of $z = 3$. Hereafter, we exclude CDFS-24 from the X-ray obscured source sample. The resulting sample contains 17 sources. Eight of the 17 X-ray obscured QSOs present NL optical spectra, while two sources are associated with BL AGN. There are no spectra available for seven sources. The redshift distribution is given in Fig. 2. All sources apart from one lie at redshift $z > 2$.

We estimate the surface density of X-ray obscured QSOs by taking the area covered by the survey at a given flux into account. We estimate a surface density of 210 deg^{-2} down to a flux of $f_{2-10} \approx 1.6 \times 10^{-15}$ erg cm^{-2} s^{-1}. Five more luminous ($L_{\rm x} > 10^{44}$ erg s^{-1}) sources present no absorption ($N_{\rm H} > 10^{22}$ cm^{-2}) and are thus classified here as X-ray unobscured QSOs (see Table 2). The surface density of X-ray unobscured QSOs is ∼60 deg^{-2} at a flux of $f_{2-10} \sim 5 \times 10^{-15}$ erg cm^{-2} s^{-1}. The ratio of X-ray obscured to unobscured QSOs is $R = 3.4 \pm 1.7$. However, at the same flux limit, $\sim 5 \times 10^{-15}$ erg cm^{-2} s^{-1},

[1] http://data.spitzer.caltech.edu/popular/goods/Documents/

Table 1. The X-ray obscured QSOs.

ID[1]	Name	$N_{\rm H}^{2}$	z^{3}	Opt. Mag.[4]	Colour[5]	$L_{\rm x}^{6}$	$f_{8\ \mu{\rm m}}^{7}$	$f_{24\ \mu{\rm m}}^{8}$	$f_{\rm x}^{9}$	X/O[10]	class[11]
6	J033302.7-274823	$4.0^{+1.6}_{-1.9}$	2.46	25.67[a]	4.17[a]	44.23	–	–	–14.40	1.36	–
24[†]	J033242.0-275203	$4.0^{+4.6}_{-4.0}$	3.610	22.40	1.45	44.42	22.7	124.3	–14.59	0.07	BL
27	J033239.8-274851	$47.8^{+8.6}_{-7.8}$	3.064	24.71	3.86	44.50	29.4	166.6	–14.37	1.21	NL
31	J033237.9-275213	$2.1^{+0.5}_{-0.6}$	1.603	24.11	4.59	44.17	259.1	1085.4	–14.06	1.28	NL
45	J033225.8-274306	$12.2^{+3.3}_{-2.8}$	2.291	25.37	4.56	44.08	158.5	535.7	–14.49	1.36	NL
54	J033214.7-275422	$18.8^{+6.1}_{-5.5}$	2.561	25.69[a]	–	44.08	5.3	–	–14.60	0.87	NL
57	J033213.0-275238	$18.8^{+5.2}_{-4.6}$	2.562	24.17	2.48	44.15	10.9	<40	–14.53	0.84	NL
61	J033210.6-274309	$2.4^{+0.7}_{-0.9}$	2.02	24.51	5.00	44.28	90.3	–	–14.08	1.42	–
62	J033209.5-274807	$23.2^{+4.5}_{-4.2}$	2.810	20.49	1.05	44.39	244.	920.2	–14.38	–0.48	BL
68	J033201.6-274327	$6.9^{+3.0}_{-3.0}$	2.726	23.99	2.11	44.27	14.9	<40	–14.35	0.94	BL
72	J033158.3-275043	$10.4^{+3.1}_{-2.2}$	1.99	>26[a]	–	44.09	–	–	–14.33	>1.56	–
76	J033152.6-275018	$19.8^{+3.8}_{-3.6}$	2.394	24.50[a]	4.64[a]	44.34	–	–	–14.28	0.72	NL
159	J033250.4-275253	$9.5^{+6.7}_{-3.8}$	3.30	24.86	3.97	44.65	30.6	190.5	–14.28	1.35	–
202	J033229.9-275106	$36.8^{+20.5}_{-15.7}$	3.700	24.54	2.82	44.12	1.0	93.1	–14.92	0.59	NL
227	J033205.4-274644	$65.4^{+22.0}_{-16.5}$	2.18	26.90	5.80	44.00	25.3	<40	–14.58	1.87	–
600[*]	J033213.9-274526	380^{+180}_{-180}	1.33	23.25	3.71	44.43	27.4	51.2	–14.58	0.41	NL
605[*]	J033239.2-274833	2700^{+3800}_{-1700}	4.29	26.27	4.11	44.95	5.4	<40	–14.92	1.27	–
610*	J033219.9-275159	520^{+580}_{-280}	2.04	27.90	6.41	44.18	21.4	<40	–15.01	1.85	–

[1] ID number from Giacconi et al. (2002). [2] Rest-frame column density in units 10^{22} cm^{-2}. [3] Redshift from: (a) Szokoly et al. (spectroscopic) or (b) Zheng et al. (photometric). [4] Optical ACS I magnitude; (a) denotes R magnitude instead. [5] $I-3.6$ colour; (a) denotes $R-K$ colour instead. [6] logarithm of 2–10 keV intrinsic luminosity (erg s^{-1}). [7] *Spitzer* IRAC 8 μm flux density (μJy). [8] *Spitzer* MIPS 24 μm flux density (μJy). [9] Absorbed 2–10 keV X-ray flux erg cm^{-2} s^{-1} as derived from the spectral fits. [10] logarithm of X-ray to optical flux ratio. [11] Optical spectroscopic classification: narrow line (NL), broad line (BL). [†] Border-line X-ray obscured QSO, consistent with $N_{\rm H} < 10^{22}$ cm^{-2} at the 90% confidence level. [*] Compton-thick sources; column densities have been derived using the plcabs model.

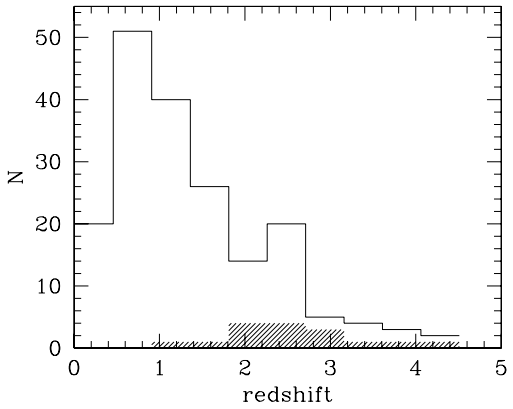

Fig. 2. The X-ray obscured QSO (hatched histogram) redshift distribution compared with the total (open).

we estimate $R \sim 1$. Four of the X-ray unobscured QSOs are associated with BL AGN, while for the other one there is no spectrum available.

3.2. Compton-thick sources

The X-ray spectral fits for the X-ray obscured QSOs are presented in Fig. 6. The X-ray spectral fits show that three sources apparently present very large amounts of rest-frame absorption ($N_{\rm H} > 10^{24}$ cm^{-2}) and are thus candidate Compton-thick sources. These are CDFS-600, 610, and 605 at redshifts 1.327, 2.04, and 4.29, respectively. We caution that the absorption model we use (*WA* in *XSPEC*) is only valid at column densities lower than 10^{24} cm^{-2} where photoelectric absorption dominates the opacity. At higher column densities, Compton scattering contributes significantly to the opacity. In these cases we have used the *PLCABS* model (Yaqoob 1997), which takes multiple Compton scattering into account and is valid for columns up to 5×10^{24} cm^{-2}. For higher columns we cannot obtain an accurate enough estimate of the column, but we can nevertheless be confident that the source is Compton-thick. CDFS-600 is associated with a NL AGN, while the other two sources only have a photometric redshift available. Another uncertainty in the determination of the column density comes from the photometric redshifts themselves. Rigby et al. (2005) point out that there might be an ambiguity in the photometric redshifts, at least in the case of optically faint sources. They present *Spitzer* photometric observations of 20 optically faint sources in the CDFS. Three of their sources coincide with X-ray obscured QSOs here: 27, 45 and 159. Rigby et al. (2005) derive photometric redshifts using the additional *Spitzer* bands. In the case of e.g. CDFS-159, they find a redshift discrepancy with that of Zheng et al. (2004) by $\delta z > 1$. In the case of Compton-thick sources, a strong 6.4 keV FeK line (equivalent width ~1 keV) is usually observed (Matt et al. 1996). Unfortunately, the spectra of the three candidate Compton-thick sources have limited statistics revealing no evidence of an Fe line. The 90% upper limits on the equivalent width of the 6.4 keV line are as high as several keV in all three cases.

In total we find 8 Compton-thick AGN when we consider all X-ray luminosities. These Compton-thick AGN are revealed directly through the detection of their absorption turnover. Such column densities cannot be detected at low redshift in the *Chandra* energy passband, as the absorption turnover occurs at energies >10 keV. At high redshift the k-correction shifts the absorption turnover at low energies. It is likely that these 8 AGN represent only a fraction of the Compton-thick sources in our sample. Indeed, at lower redshifts or higher column densities,

Table 2. X-ray unobscured QSOs.

ID[1]	Name	N_H^2	z^3	Opt. Mag.[4]	Colour[5]	L_x^6	$f_{8\,\mu m}^7$	$f_{24\,\mu m}^8$	f_x^9	X/O[10]	class[11]
11	J033260.0-274748	<0.2	2.579	21.83[a]	2.73[a]	44.54	–	–	–14.15	0.08	BL
22	J033243.3-274915	<0.2	1.920	22.54	1.97	44.16	32.4	152.7	–14.30	0.41	BL
42	J033227.1-274105	<0.02	0.73	19.11	1.70	44.25	661.5	999.7	–13.20	0.14	–
60	J033211.0-274415	<0.10	1.615	22.37	2.53	44.22	93.9	285.7	–14.05	0.59	BL
67	J033202.5-274601	<0.43	1.616	23.73	3.84	44.06	49.4	258.0	–14.16	1.03	BL

[1] ID number from Giacconi et al. (2002). [2] Rest-frame column density in units 10^{22} cm^{-2}. [3] Redshift from: (a) Szokoly et al. (spectroscopic) or (b) Zheng et al. (photometric). [4] Optical ACS I magnitude; (a) denotes R magnitude instead. [5] $I-3.6$ colour; (a) denotes $R-K$ colour instead. [6] logarithm of 2–10 keV intrinsic luminosity (erg s^{-1}). [7] *Spitzer* IRAC 8 μm flux density (μJy). [8] *Spitzer* MIPS 24 μm flux density (μJy). [9] logarithm of absorbed 2–10 keV X-ray flux erg cm^{-2} s^{-1} as derived from the spectral fits. [10] logarithm of X-ray to optical flux ratio. [11] Optical Spectroscopic classification: narrow line (NL), broad line (BL).

the column density cannot be detected directly. Instead, the spectrum will appear flat. We have thus looked for cases where leaving the spectral index free results in a very flat spectrum: $\Gamma \sim 1$ or flatter with $\Delta C = 2.7$. We find ten such cases, raising the total number of candidate Compton-thick sources to 18 (see Table 3).

3.3. X/O ratio and optical-IR colour

The optical (I or R) magnitudes and X-ray to optical flux ratios, X/O, are presented in Table 1. Four X-ray obscured QSOs fall outside the ACS survey. For these we present R magnitudes from VLT/FORS instead. For CDFS-72 there is only a magnitude lower limit as this was not detected at the limit of the FORS observations ($R = 26$). The X/O is defined as the ratio of the 2–10 keV flux to optical (I band) flux:

$$X/O = \log(f_x/f_o) = 5.7 + \log f_x + I/2.5. \quad (1)$$

In the case where we only have R magnitudes available the X/O ratio is estimated using the equation in Hornschemeier et al. (2003). Three sources (CDFS-6, 72, 76) have not been covered by the *Spitzer* IRAC survey and 5 sources have not been covered by MIPS (CDFS-6, 72, 76, 61, 54). All X-ray obscured QSOs that lie within the IRAC field-of-view have been detected at 8 μm. Instead only seven have been detected by MIPS at 24 μm. Finally, the $I-3.6$ μm colour is given in Table 1. The 3.6 μm magnitude is estimated from the relation

$$m_{3.6\,\mu m} = -2.5\ \log f_{3.6\,\mu m} + 23.9 \quad (2)$$

where the flux $f_{3.6}$ is in units of μJy. The X/O ratio as a function of the $I-3.6$ μm colour is given in Fig. 3. There is a strong correlation between the X/O and the $I-3.6$ μm colour in the sense that the redder sources present high X/O. All the high X/O sources (X/O > 1 or Extreme X/O sources EXO) have $I-3.6$ μm > 4. This colour is roughly equivalent to an ERO defined as having $R-K > 5$. However, not all X-ray obscured QSOs are EXOs or EROs. Conversely, one of the X-ray unobscured QSOs is an EXO (CDFS-67).

3.4. Mid-IR properties

Additional clues to the nature of the X-ray obscured QSOs can be provided by their mid-IR properties. The X-ray to mid-IR flux ratios provide a useful diagnostic for identifying obscured AGN. Unobscured AGN have ratios around unity (e.g. Lutz et al. 2004). In Fig. 4 we present the absorbed X-ray flux against the IRAC 8 μm (left panel) and 24 μm (right panel) flux density for all X-ray sources. The region occupied by the hard X-ray selected AGN in the HEAO-1 sample of Piccinotti et al. (1982) is

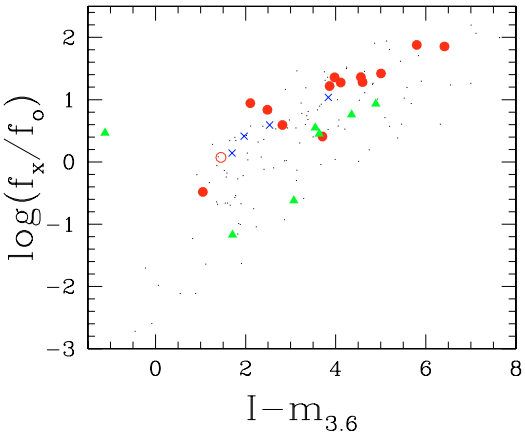

Fig. 3. The logarithm of the X-ray to optical flux ratio or X/O as a function of the $I-3.6$ μm colour. X-ray obscured and unobscured QSOs are denoted with filled circles and crosses respectively. The open circle denotes the border-line X-ray obscured QSO CDFS-24. The remaining sources are shown as dots.

also shown. There are four X-ray obscured QSOs that lie below the AGN locus of points in the 24 μm diagram. The same X-ray obscured QSOs have low X-ray fluxes relative to their 8 μm flux densities. These are associated with a BL QSO (CDFS-62), and three NL QSOs (CDFS-202, CDFS-45, CDFS-31). These have less X-ray emission for their mid-IR flux density, and thus they should be associated with the most heavily absorbed sources. Surprisingly, none of the candidate Compton-thick sources are among these. The BL QSO CDFS-62 presents no evidence of reddening in the optical having $I-3.6 \approx 1$. In contrast, sources CDFS-45 and CDFS-31 have $I-3.6 > 4$ being among the redder sources in our sample. CDFS-202 presents little reddening with $I-3.6 = 2.8$. Norman et al. (2002) present the properties of this NL QSO in detail at a redshift of 3.7.

In the mid-IR, AGN present red, featureless spectra (Hao et al. 2005). Thus the mid-IR colours can provide a powerful tool to identify AGN (Lacy et al. 2004; Stern et al. 2004; Hatziminaoglou et al. 2005). In Fig. 5 we plot the mid-IR colours of our sample with the "red" region empirically defined by Lacy et al. (2004) to contain luminous AGN. Lacy et al. find that the normal galaxies lie in the blue part of the diagram with colours clustering around [8.0]–[4.5] = −0.5 and [5.8]–[3.6] = −0.5. The vast majority of our X-ray selected of QSOs are "red". The only source lying outside (albeit only marginally) the red AGN region defined by Lacy et al. is CDFS-600.

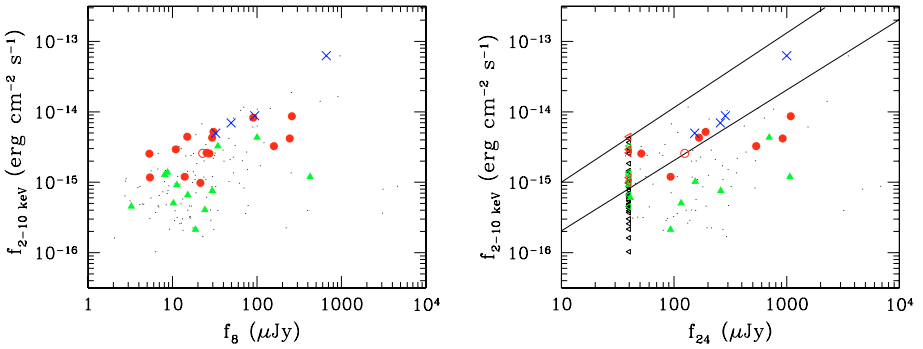

Fig. 4. The 2–10 keV absorbed X-ray flux versus the *Spitzer* IRAC 8 μm (*left panel*) and MIPS 24 μm monochromatic flux for hard X-ray selected sources in the CDFS. X-ray obscured and unobscured QSOs are denoted with filled circles and crosses respectively; open squares represent the Compton-thick AGN; the remaining sources are shown as dots; triangles denote 24 μm luminosity upper limits. The solid lines in the right panel denote the region occupied by the Piccinotti AGN sample (see Alonso-Herrero et al. 2004).

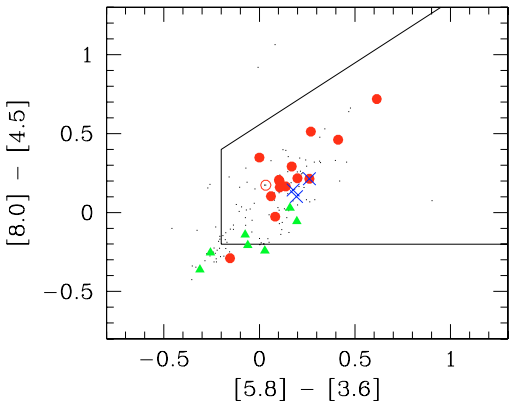

Fig. 5. *Spitzer* IRAC colours. We denote with solid lines the region which is used as an AGN diagnostic tool in mid-IR according to Lacy et al. Symbols as in Fig. 3.

4. Discussion

We have derived the X-ray spectral properties for all 186 hard extragalactic (2–10 keV) X-ray selected sources within the central field-of-view of the CDF-S. We use strictly X-ray criteria to define X-ray obscured QSOs, regardless of their optical spectrum, as those having high unobscured luminosities $L_x > 10^{44}$ erg s^{-1} and high obscuration column density $N_H > 10^{22}$ cm^{-2}. We find 17 X-ray obscured QSOs among the 186 sources. The ratio of X-ray unobscured to X-ray obscured QSOs ($L_x > 10^{44}$ erg s^{-1}) is 3.4 ± 1.7. This is consistent with the ratio at lower luminosities ($L_x < 10^{44}$ erg s^{-1}) which is $R \approx 2.5 \pm 0.5$. At first this is at odds with recent findings that show that the fraction of obscured AGN decreases significantly at high luminosities: Ueda et al. (2003), La Franca et al. (2005), Akylas et al. (2006) find ratios, R, well below unity, at high luminosities. This apparent discrepancy could be attributed to the fact that we are using a pencil-beam flux limited survey, so we cannot probe large enough volumes to detect a high number of luminous unobscured QSOs (see also the discussion by La Franca et al. 2005 and Akylas et al. 2006).

The optical spectra of the X-ray obscured QSOs show that these comprise a mixed bag of objects. Eight sources present NL spectra, two are associated with BL AGN, while for seven more there are no spectra available. The BL source CDFS-062 presents a high column, 2×10^{23} cm^{-2}. This column should correspond to $A_V \sim 100$ using the Galactic dust-to-gas ratio (Bohlin et al. 1978) or equivalently to $A_{2000\ Å} \sim 300$ mag in the UV (Richards et al. 2003). In reality, CDF-062 has a broad CIII] emission line implying that the reddening must be negligible. Such peculiar BL AGN with high X-ray obscuration but little optical reddening have often been reported in the literature (e.g. Elvis et al. 1998; Maiolino et al. 2001; Georgantopoulos et al. 2003; Perola et al. 2004; Akylas et al. 2004). It is possible that some of the absorption may be intervening. The most prominent and well-studied case of BL QSOs with large amounts of X-ray absorption are the Broad Absorption Line (BAL) QSOs. Although the X-ray spectra of BAL are usually absorbed by X-ray column densities of 10^{23} cm^{-2} (e.g. Gallagher et al. 2001), they present only a small amount of optical reddening (Brotherton et al. 2001). The optical spectrum of CDF-062 presents prominent, blueshifted absorption lines of CIV and SiIV with an *FWHM* of about 5.000 km s^{-1}. The absorption line widths are clearly less than those typical of BAL QSOs. This suggests that a fraction of the X-ray absorbed BL QSOs may be associated with a population of such "mini-BAL" QSOs. CDFS-24 and 68 also show evidene of blueshifted absorption lines.

A large fraction of our X-ray obscured QSOs have high X/O ratios. Fiore et al. (2003) postulate that this is because the nuclear emission is obliterated by dust at high redshift. The same high X/O sources show very red colours having $I - 3.6\ \mu m > 4$ and can be classified as EROs. Indeed it has been shown that X-ray detected EROs have high X/O ratios (Lehmann et al. 2001; Alexander et al. 2001; Brusa et al. 2005). It is likely that these EROs have red colours because they are associated with elliptical galaxies at high redshift. The high X/O ratios can be explained as, on one hand, the optical nuclear light being attenuated, while the X-ray emission emerges relatively unscathed on the other hand. Despite the very strong correlation between the X/O ratio and the $I - 3.6$ colour there are some EROs that have X/O ratios characteristic of normal AGN, X/O ∼ 0, (see also Koekomoer et al. 2004). It is important to stress that not all X-ray obscured QSOs are red or high X/O sources. For example, the X-ray obscured QSO CDFS-202 (Norman et al. 2002) has bluish colours with $I - 3.6 = 2.8$, or $R - K = 2.5$. Norman et al. (2002) assert that the blue colour is because of a strong emission line in the R filter. Nevertheless, the $I - 3.6$ colour of CDFS-202 is blue as well.

All X-ray obscured QSOs observed by IRAC, were detected at 8 μm. In contrast, less than half were detected at 24 μm. The X-ray to mid-IR diagram can provide additional information on which sources have large intrinsic columns: an absorbed source should have a low ratio of absorbed to mid-IR flux provided that the latter is an isotropic indicator of the nuclear emission. Only four sources appear to be absorbed according to the above criterion. Then, by comparison, the X/O ratio or the $I-3.6$ colour provide a rather more efficient diagnostic for separating X-ray obscured AGN. This may be attributed to the high redshifts of our sources. Fadda et al. (2002) argue that, at high redshift, the X-ray to mid-IR flux may increase rapidly, as the IR flux corresponds

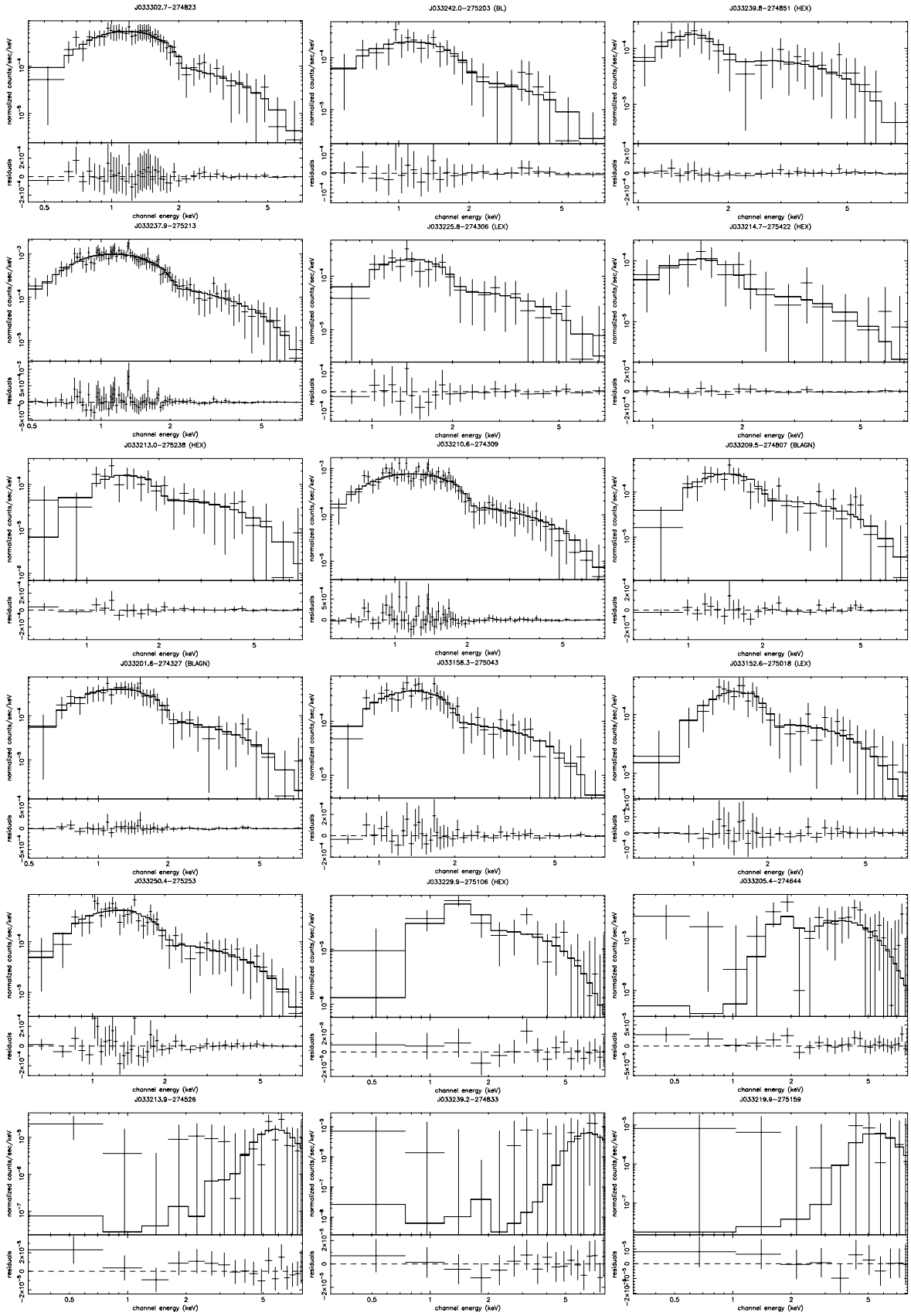

Fig. 6. Power-law fits and χ^2 residuals to the spectra of the X-ray obscured QSOs.

to shorter wavelengths, while the X-ray flux is less affected by photoelectric absorption. Nevertheless, the X-ray to mid-IR flux ratio may provide a complementary tool to the X/O ratio and $I-3.6$ colour. Indeed, among the four sources with low X-ray to mid-IR ratio, CDFS-62 and CDF-202 have neither red colour nor a high X/O ratio.

Lacy et al. (2004) demonstrate that the mid-IR colours can be efficiently used to separate AGN from normal galaxies. In particular Lacy et al. argue that the AGN have relatively red mid-IR colours (5.8–3.6 against 8.0–4.5 μm) compared with normal galaxies. Barmby et al. (2006) argue that the X-ray selected AGN in the Extended Groth Strip Survey (EGS) occupy both blue and red mid-IR colours, so that such colours cannot be used efficiently to separate them from normal galaxies. In our case we find that the mid-IR diagnostics used by Lacy et al. provide a very powerful diagnostic for the selection of X-ray obscured QSOs. Only one of our X-ray obscured QSOs lies outside the AGN region (albeit marginally). The discrepancy with the findings of Barmby et al. probably arises because we are only dealing with luminous AGN. The EGS sources of Barmby et al. span a wide range of luminosities: so it is possible that the mid-IR colours of the less luminous sources (Seyfert-like luminosities) are contaminated by the host galaxy.

The X-ray spectral fits show that three of the X-ray obscured QSOs are Compton-thick sources. Two of the Compton-thick sources present high X/O and red colour. The number of Compton-thick sources amounts to 18 (or about 10% of all sources) if we consider all X-ray luminosities. This figure is roughly consistent with the predictions of Comastri et al. (2001) for the number of Compton-thick sources at these flux levels (about 7% at 5×10^{-16} erg cm^{-2} s^{-1}). The predictions of Comastri et al. (2001) are based on the distribution of the column densities observed in the local Universe by Risaliti et al. (1999). Our work substantially increases the number of known Compton-thick sources at high redshifts. Other examples of Compton-thick sources at high redshift include the four sources at $z > 2$ from the sub-mm selected sample of Alexander et al. (2005) and the NL QSO at $z = 3.288$ from the Lynx field (Stern et al. 2002). Moreover, two additional NL QSOs in the CDFS have been reported as Compton-thick: CDFS-202 (Norman et al. 2002) and CDFS-263 (Mainieri et al. 2005). Our spectral fits place these sources marginally outside the $N_{\rm H} > 10^{24}$ cm^{-2} regime. Nevertheless, these are still consistent with being Compton-thick given the spectral fit uncertainties. Moreover, the adopted slope of the photon index affects the derived $N_{\rm H}$ significantly. Polletta et al. (2006) report the discovery of two Compton-thick QSOs at redshifts $z = 2.54$ and 2.43 in the Chandra/SWIRE survey in the Lockman Hole.

Just before the submission of this paper, Tozzi et al. (2006) presented an analysis of the X-ray spectral properties of all 321 extragalactic sources in the CDFS. They find 14 Compton-thick sources, defined as having a reflection dominated spectrum. In particular, Tozzi et al. use the *PEXRAV* model in XSPEC to fit the spectra of these 14 sources. Interestingly, the Compton-thick samples of Tozzi et al. and ours show little overlap: only sources CDFS-153, 505, 531 and 610 are common. However, Tozzi et al. do not include the sources that present column densities $N_{\rm H} > 10^{24}$ cm^{-2}, in their Compton-thick sample i.e. CDFS-599, 600, 601, 605, 609, 634. This would alleviate the discrepancy between the two samples. Finally, there are sources in their sample that show very flat spectral index, e.g. CDFS-25 with $\Gamma = 0.29^{+0.21}_{-0.20}$, which should be considered as candidate Compton-thick sources.

5. Conclusions

We have explored the X-ray optical and mid-IR properties of X-ray obscured QSOs on the CDFS. We classify X-ray obscured QSOs on the basis of purely X-ray criteria i.e. high luminosity $L_{\rm x} > 10^{44}$ erg s^{-1} combined with high hydrogen column density $N_{\rm H} > 10^{22}$ cm^{-2}. We are selecting X-ray obscured through the 186 hard extragalactic X-ray sources that lie in the central FOV of the CDFS. We have derived proper X-ray spectra (instead of hardness ratios) for all our sources. Photometric or spectroscopic redshifts exist for the vast majority of the sources (185 out of 186) ascertaining that optical selection biases are of no importance in our study. We find 17 X-ray obscured QSOs spanning the redshift range 1.3–4.2. Our main results can be summarised as follows:

1. The surface density of X-ray obscured QSOs is 210 deg^{-2} at $f_{2-10} \sim 10^{-15}$ erg cm^{-2} s^{-1}.
2. Our X-ray obscured QSO sample comprises of sources with both NL and BL spectra. The BL source with the highest absorption (10^{23} cm^{-2}) is a mini-BAL.
3. Three out of 17 X-ray obscured QSOs present very high column densities ($>10^{24}$ cm^{-2}) and are classified as Compton-thick QSOs. When considering all luminosities, we classify 18 sources as candidate Compton-thick AGN, based on the detection of either high column densities or flat X-ray spectra.
4. About half of our X-ray obscured QSOs present a very high X-ray to optical flux ratio, X/O > 1. These present very red colours ($I - 3.6\,\mu$m) and most can be classified as EROs.
5. The X-ray to mid-IR flux ratio can provide a complementary tool for selecting heavily obscured sources. Four out of 17 X-ray obscured QSOs appear to have a low X-ray to mid-IR flux ratio; only two of these four sources have either a red colour or a high X/O ratio.
6. Practically all 17 QSOs have red mid-IR colours and can be very easily separated from the normal galaxies detected in mid-IR, as pointed out by Lacy et al. (2004). This suggests that the mid-IR selection provides a powerful tool for detecting obscured QSOs at high redshift.

Acknowledgements. We are grateful to the anonymous referee for the numerous corrections and suggestions. We acknowledge use of ESO/GOODS data. The Chandra data were taken from the Chandra Data Archive at the Chandra X-ray Center.

References

Akylas, A., Georgakakis, A., & Georgantopoulos, I. 2004, MNRAS, 353, 1015
Akylas, A., Georgantopoulos, I., & Georgakakis, A. 2006, A&A, in press
Alexander, D. M., Brandt, W. N., Hornschemeier, A. E., et al. 2001, AJ, 122, 2156
Alexander, D. M., Bauer, F. E., Brandt, W. N., et al. 2003, AJ, 126, 539
Alexander, D. M., Bauer, F. E., Chapman, S. C., et al. 2005, ApJ, 632, 736
Alonso-Herrero, A., Pérez-González, P. G., Rigby, J., et al. 2004, ApJS, 54, 155
Barger, A. J., Cowie, L. L., Capak, P., et al. 2003, AJ, 126, 632
Barmby, P., Alonso-Herrero, A., Donley, J. L., et al. 2006, ApJ, submitted
Bohlin, R. C., Savage, B. D., & Drake, J. F. 1978, ApJ, 224, 132
Brandt, W. N., & Hasinger, G. 2005, ARA&A, 43, 827
Brotherton, M. S., Tran, H. D., Becker, R. H., et al. 2001, ApJ, 546, 775
Brusa, M., Comastri, A., Daddi, E., et al. 2005, A&A, 432, 69
Cash, W. 1979, ApJ, 228, 939
Comastri, A., Fiore, F., Vignali, C., et al. 2001, MNRAS, 327, 781
Dickey, J. M., & Lockman, F. J. 1990, ARA&A, 28, 215
Elvis, M., Fiore, F., Giommi, P., & Padovani, P. 1998, ApJ, 492, 91
Fadda, D., Flores, H., Hasinger, G., et al. 2002, A&A, 383, 838
Fazio, G. G., Hora, J. L., Allen, L. E., et al. 2004, ApJS, 154, 10
Fiore, F., Brusa, M., Cocchia, F., et al. 2003, A&A, 409, 79
Gallagher, S. C., Brandt, W. N., Laor, A., et al. 2001, ApJ, 546, 795
Georgantopoulos, I., Georgakakis, A., Stewart, G. C., et al. 2003, MNRAS, 342, 321

Giacconi, R., Zirm, A., & Wang, J. 2002, ApJS, 139, 369
Giavalisco, M., Ferguson, H. C., Koekemoer, A. M., et al. 2004, ApJ, 600, L93
Hao, L., Spoon, H. W. W., Sloan, G. C., et al. 2005, ApJ, 625, 75
Hatziminaoglou, E., Perez-Fournon, I., Polletta, M., et al. 2005, AJ, 129, 1198
Hornschemeier, A. E., et al. 2003, AJ, 126, 575
Kashikawa, N., Shimasaku, K., Yasuda, N., et al. 2004, PASJ, 56, 1011
Koekemoer, A. M., Alexander, D. M., Bauer, F. E., et al. 2004, ApJ, 600, L123
Lacy, M., Storrie-Lombardi, L. J., Sajina, A., et al. 2004, ApJS, 154, 166
La Franca, F., Fiore, F., Comastri, A., et al. 2005, ApJ, 635, 864
Lehmann, I., Hasinger, G., Schmidt, M., et al. 2001, A&A, 371, 833
Lutz, D., Maiolino, R., Spoon, H. W. W., & Moorwood, A. F. M. 2004, A&A, 418, 465
Mainieri, V., Rigopoulou, D., Lehmann, I., et al. 2005a, MNRAS, 356, 1571
Mainieri, V., Rosati, P., Tozzi, P., et al. 2005b, A&A, 437, 805
Maiolino, R. Marconi, A., Salvati, M., et al. 2001, A&A, 265, 28
Matt, G., Fiore, F., Perola, G. C., et al. 1996, MNRAS, 281, L69
Norman, C., Hasinger, G., Giacconi, R., et al. 2002, ApJ, 571, 218
Padovani, P., Allen, M. G., Rosati, P., & Walton, N. A. 2004, A&A, 424, 545
Perola, G. C., Puccetti, S., Fiore, F., et al. 2004, A&A, 421, 491
Piccinotti, G., Mushotzky, R. F., Boldt, E., et al. 1982, ApJ, 253, 485
Polletta, M., Wilkes, B. J., Siana, B., et al. 2006, ApJ, in press [arXiv:astro-ph/0602228]
Rieke, G. H., Young, E. T., & Engelbracht, C. W. 2004, ApJS, 154, 25
Rigby, J. R., Rieke, G. H., Pérez-González, P. G., et al. 2005, ApJ, 627, 134
Risaliti, G., Maiolino, R., & Salvati, M. 1999, ApJ, 522, 157
Rosati, P., Tozzi, P., Giacconi, R., et al. 2002, ApJ, 566, 667
Steffen, A. T., Barger, A. J., Cowie, L. L., Mushotzky, R. F., & Yang, Y. 2003, ApJ, 596, L23
Stern, D., Moran, E. C., Coil, A. L., et al. 2002, ApJ, 568, 71
Stern, D., Eisenhardt, P., & Gorjian, V. 2005, ApJ, 631, 163
Szokoly, G. P., Bergeron, J., Hasinger, G., et al. 2004, ApJS, 155, 271
Tozzi, P., Gilli, R., Mainieri, V., et al. 2006, A&A, 451, 457
Treister, E., Urry, C. M., Chatzichristou, E., et al. 2004, ApJ, 616, 123
Ueda, Y., Akiyama, M., Ohta, K., et al. 2003, ApJ, 598, 886
Werner, M. W. 2004, ApJS, 154, 1
Yaqoob, T. 1997, ApJ, 479, 184
Zheng, W., Mikles, V. J., Mainieri, V., et al. 2004, ApJS, 155, 73

Online Material

Table 3. Spectral fits.

ID	Name[1]	Γ[2]	$N_{\rm H}$[3]	$L_{\rm x}$[4]	Class[5]	z[6]	flux[7]	χ^2/d.o.f.
3	J033306.0-274651	1.80	$0.86^{+0.32}_{-0.29}$	41.52	Galaxy	0.22	0.21	–
4	J033303.7-274519	$1.93^{+0.20}_{-0.15}$	<0.43	43.50	–	1.260	0.34	0.90
6	J033302.7-274823	$2.25^{+0.28}_{-0.19}$	$4.02^{+1.61}_{-1.88}$	44.23	–	2.46	0.39	0.63
10	J033259.9-274627	1.80	$2.71^{+0.53}_{-0.48}$	42.55	LEX	0.424	0.51	–
11	J033260.0-274748	$1.97^{+0.11}_{-0.09}$	<0.59	44.54	BLAGN	2.579	0.71	1.16
12	J033259.8-275031	$2.20^{+0.21}_{-0.18}$	<0.07	41.69	ABS	0.251	0.22	1.00
15	J033253.0-275120	$1.91^{+0.08}_{-0.22}$	$0.42^{+0.50}_{-0.42}$	43.51	BLAGN	1.23	0.37	1.11
17	J033249.3-275505	1.80	$0.42^{+0.68}_{-0.42}$	42.62	-	0.87	0.11	–
18	J033248.0-274233	$1.98^{+0.09}_{-0.10}$	$2.44^{+0.49}_{-0.37}$	43.92	LEX	0.979	1.66	0.81
20	J033244.5-274941	1.80	$6.51^{+1.68}_{-1.48}$	43.20	–	1.016	0.28	–
21	J033244.4-275252	1.80	<2.64	43.81	BLAGN	3.471	0.07	–
22	J033243.3-274915	$1.92^{+0.16}_{-0.12}$	<0.68	44.16	BLAGN	1.92	0.50	0.77
23	J033242.0-274400	1.80	<0.21	42.80	–	0.73	0.25	–
24	J033242.0-275203	1.80	$4.02^{+4.59}_{-4.02}$	44.42	BLAGN	3.610	0.26	–
25*	J033240.9-275548	$0.57^{+0.39}_{-0.37}$	$0.38^{-0.30}_{+0.30}$	42.88	ABS	0.625	0.43	–
26	J033239.8-274612	1.80	$4.63^{+1.98}_{-1.72}$	43.56	–	1.65	0.21	–
27	J033239.8-274851	1.80	$47.95^{+8.61}_{-7.79}$	44.50	HEX	3.064	0.44	–
28	J033239.2-274602	1.80	$1.24^{+0.99}_{-0.83}$	43.16	BLAGN	1.216	0.17	–
29	J033239.0-275701	$2.02^{+0.16}_{-0.19}$	$4.47^{+0.92}_{-0.82}$	42.69	–	0.30	1.54	1.18
31	J033237.9-275213	$2.22^{+0.11}_{-0.14}$	$2.14^{+0.50}_{-0.63}$	44.17	HEX	1.603	0.87	0.83
33	J033236.8-274407	$1.75^{+0.11}_{-0.16}$	$0.12^{+0.16}_{-0.12}$	43.11	LEX	0.67	0.64	0.93
34	J033235.0-275512	1.80	$0.86^{+0.40}_{-0.40}$	43.00	–	0.839	0.29	–
36	J033233.1-274548	1.80	$0.38^{+0.21}_{-0.17}$	41.90	–	0.33	0.20	–
37	J033232.2-274156	1.80	$0.54^{+0.89}_{-0.54}$	42.72	–	0.96	0.11	–
38	J033230.3-274505	$2.13^{+0.12}_{-0.11}$	<0.17	43.13	BLAGN	0.74	0.52	1.27
39	J033230.1-274530	$1.87^{+0.08}_{-0.08}$	<0.33	43.91	BLAGN	1.22	0.95	1.19
41	J033227.7-274145	1.80	$7.78^{+1.32}_{-1.21}$	43.11	HEX	0.667	0.63	–
42	J033227.1-274105	$2.09^{+0.03}_{-0.03}$	0.17	44.25	–	0.73	6.31	1.25
43	J033226.9-274146	1.80	$2.91^{+0.81}_{-0.73}$	42.84	LEX	0.737	0.27	–
44	J033226.6-274036	$2.44^{+0.09}_{-0.08}$	<0.26	43.59	–	1.031	0.68	1.12
45	J033225.8-274306	1.80	$12.21^{+3.29}_{-2.82}$	44.08	LEX	2.291	0.33	–
46	J033225.3-274219	$2.23^{+0.29}_{-0.29}$	$0.77^{+0.90}_{-0.77}$	43.59	BLAGN	1.617	0.23	1.34
47	J033225.1-274101	1.80	$7.22^{+1.84}_{-1.80}$	42.86	LEX	0.733	0.28	–
48	J033224.9-275601	1.80	$5.55^{+1.48}_{-1.30}$	43.43	–	1.26	0.30	–
49	J033224.3-274127	1.80	<0.15	42.49	LEX	0.534	0.26	–
50*	J033219.1-274756	$1.01^{+0.53}_{-0.47}$	$0.13^{+0.32}_{-0.13}$	42.45	ABS	0.67	0.14	–
51	J033217.3-275221	$2.69^{+0.28}_{-0.44}$	$30.14^{+5.07}_{-8.21}$	43.76	–	1.097	0.87	1.27
52	J033217.2-274304	$2.03^{+0.16}_{-0.12}$	<0.13	42.80	BLAGN	0.569	0.45	0.80
53	J033215.1-275128	1.80	<0.08	42.69	BLAGN	0.675	0.24	–
54	J033214.7-275422	1.80	$18.80^{+6.08}_{-5.50}$	44.08	HEX	2.561	0.25	–
55	J033214.1-275101	1.80	$1.86^{+0.32}_{-0.30}$	41.37	HEX	0.122	0.51	–
56	J033213.3-274241	$1.49^{+0.19}_{-0.15}$	$2.05^{+0.73}_{-0.45}$	43.25	–	0.605	1.12	0.93
57	J033213.0-275238	1.80	$18.80^{+5.21}_{-4.63}$	44.15	HEX	2.562	0.29	–
58	J033211.8-274629	1.80	$2.76^{+1.01}_{-0.90}$	42.94	–	0.92	0.20	–
59	J033211.5-275214	$1.74^{+0.18}_{-0.18}$	$1.81^{+0.84}_{-0.60}$	43.36	–	0.97	0.46	0.68
60	J033211.0-274415	$1.92^{+0.12}_{-0.09}$	<0.51	44.22	BLAGN	1.615	0.89	1.19
61	J033210.6-274309	$2.02^{+0.10}_{-0.12}$	$2.43^{+0.75}_{-0.94}$	44.28	–	2.02	0.83	0.90
62	J033209.5-274807	1.80	$23.20^{+4.50}_{-4.16}$	44.39	BLAGN	2.810	0.42	–
63	J033208.7-274735	$1.93^{+0.03}_{-0.03}$	<0.04	43.82	BLAGN	0.544	5.21	1.33
64	J033208.1-274658	$1.59^{+0.17}_{-0.17}$	$0.21^{+0.18}_{-0.11}$	41.37	–	0.13	0.46	1.44
65	J033204.0-275330	1.80	$0.50^{+0.57}_{-0.50}$	43.10	–	1.10	0.19	–
66	J033203.7-274604	1.80	$8.99^{+1.26}_{-1.16}$	43.22	LEX	0.574	1.17	–

Table 3. continued.

ID	Name[1]	Γ[2]	$N_{\rm H}$[3]	$L_{\rm x}$[4]	Class[5]	z[6]	flux[7]	χ^2/d.o.f.
67	J033202.5-274601	$1.75^{+0.13}_{-0.12}$	<0.51	44.06	BLAGN	1.616	0.69	0.76
68	J033201.6-274327	$2.15^{+0.28}_{-0.22}$	$6.87^{+2.95}_{-2.95}$	44.27	BLAGN	2.726	0.45	0.79
70	J033201.5-274648	$0.88^{+0.53}_{-0.28}$	$8.11^{+6.60}_{-4.06}$	43.78	–	1.07	0.96	1.83
72	J033158.3-275043	$2.15^{+0.19}_{-0.21}$	$10.38^{+3.10}_{-2.19}$	44.09	-	1.99	0.46	1.12
73	J033158.2-274834	1.80	$0.77^{+0.30}_{-0.30}$	42.93	LEX	0.734	0.34	–
76	J033152.6-275018	1.80	$19.82^{+3.81}_{-3.56}$	44.34	LEX	2.394	0.53	–
77	J033301.7-274543	1.80	<0.25	42.45	BLAGN	0.622	0.16	–
78	J033230.1-274524	$1.97^{+0.11}_{-0.10}$	<0.24	43.48	BLAGN	0.960	0.62	1.30
79	J033238.1-274627	1.80	<1.25	43.41	–	1.82	0.12	–
80	J033211.0-274857	1.80	<0.56	43.33	–	1.70	0.12	–
81	J033226.0-274515	1.80	$5.03^{+5.32}_{-4.14}$	43.61	–	2.59	0.08	–
82	J033214.9-275104	1.80	$10.32^{+6.33}_{-4.99}$	43.37	–	1.89	0.10	–
83	J033215.0-274225	1.80	$0.29^{+1.33}_{-0.29}$	43.49	–	1.76	0.15	–
84	J033246.9-274212	1.80	<0.04	40.63	ABS	0.10	0.13	–
85	J033244.7-274836	1.80	$9.17^{+6.51}_{-5.32}$	43.68	LEX	2.593	0.10	–
86	J033233.9-274521	1.80	$30.09^{+34.27}_{-24.24}$	43.55	–	3.09	0.05	–
89	J033208.3-274153	1.80	<1.08	43.33	BLAGN	2.47	0.05	–
91	J033242.9-274703	1.80	$3.12^{+5.35}_{-3.12}$	43.95	BLAGN	3.19	0.11	–
93	J033202.4-275235	1.80	$0.64^{+1.91}_{-0.64}$	42.79	–	1.30	0.06	–
95	J033229.9-274425	1.80	<0.02	40.15	LEX	0.08	0.09	–
96	J033220.9-275223	1.80	$0.23^{+0.43}_{-0.23}$	41.15	Galaxy	0.27	0.06	–
99	J033205.2-275356	$1.60^{+0.26}_{-0.20}$	$0.65^{+0.70}_{-0.42}$	43.04	–	0.79	0.36	1.53
101	J033255.6-274752	1.80	<0.51	43.19	–	1.625	0.09	–
103	J033228.9-274356	1.80	<0.10	41.16	ABS	0.21	0.10	–
108	J033205.8-274447	1.80	<0.48	42.91	–	1.56	0.05	–
110	J033258.7-274633	1.80	<0.57	41.85	LEX	0.622	0.04	–
114*	J033207.7-275214	$1.02^{+0.26}_{-0.26}$	<0.07	43.45	–	1.72	0.15	–
116	J033230.1-274405	1.80	0.04	40.11	LEX	0.08	0.08	–
117	J033203.1-274450	1.80	$1.75^{+3.79}_{-1.75}$	43.69	HEX	2.573	0.10	–
122	J033257.7-274549	1.80	$1.80^{+3.21}_{-1.80}$	43.41	–	2.10	0.08	–
132	J033244.1-275456	1.80	$2.67^{+2.67}_{-1.89}$	42.45	LEX	0.908	0.07	–
133	J033202.6-274430	1.80	$3.52^{+3.35}_{-2.45}$	42.80	–	1.21	0.08	–
145	J033222.6-274604	1.80	$15.08^{+4.88}_{-4.20}$	43.50	–	1.50	0.23	–
146*	J033247.2-275335	$1.02^{+0.56}_{-0.30}$	<0.31	43.83	–	2.67	0.13	–
147	J033246.4-274632	1.80	$25.02^{+7.87}_{-5.95}$	43.23	–	0.99	0.33	–
148	J033235.3-275319	1.80	$13.01^{+5.20}_{-4.19}$	43.56	–	1.74	0.18	–
149*	J033212.3-274621	$0.03^{+0.61}_{-0.64}$	<0.24	42.64	LEX	1.03	0.08	–
150	J033225.3-275451	1.80	$27.79^{+10.51}_{-7.83}$	43.11	ABS	1.090	0.20	–
151	J033220.6-274733	1.80	$19.84^{+5.91}_{-4.48}$	42.74	LEX	0.604	0.34	–
152	J033259.4-274859	1.80	$21.14^{+3.91}_{-3.46}$	43.66	–	1.28	0.48	–
153*	J033218.4-275056	$-0.38^{+0.77}_{-0.28}$	<1.4	43.68	HEX	1.536	0.33	–
155	J033208.0-274240	1.80	$1.63^{+1.37}_{-0.99}$	42.03	LEX	0.545	0.08	–
156	J033213.3-275530	1.80	$64.34^{+21.71}_{-16.76}$	43.42	ABS	1.185	0.33	–
159	J033250.4-275253	$1.64^{+0.17}_{-0.16}$	$9.54^{+6.68}_{-3.82}$	44.65	–	3.30	0.53	1.28
170	J033246.5-275414	1.80	$0.50^{+1.53}_{-0.50}$	41.98	ABS	0.664	0.05	–
171	J033235.2-274411	1.80	<1.36	41.89	LEX	0.84	0.02	–
183	J033234.2-275641	1.80	$1.79^{+1.97}_{-1.01}$	40.06	–	0.08	0.06	–
184	J033248.3-275257	1.80	$7.16^{+8.99}_{-4.51}$	42.32	ABS	0.667	0.10	–
185	J033211.0-274343	1.80	$7.25^{+8.45}_{-4.74}$	42.24	–	0.93	0.04	–
188	J033222.6-274950	1.80	$7.01^{+5.13}_{-3.38}$	42.26	LEX	0.734	0.07	–
189*	J033245.9-274213	$0.68^{+0.86}_{-0.76}$	<0.40	42.06	–	0.755	0.04	–
190	J033236.0-274100	1.80	$17.69^{+8.72}_{-5.43}$	42.79	LEX	0.733	0.24	–

Table 3. continued.

ID	Name[1]	Γ[2]	$N_{\rm H}$[3]	$L_{\rm x}$[4]	Class[5]	z[6]	flux[7]	χ^2/d.o.f.
200	J033255.0-274506	1.80	$2.40^{+1.12}_{-0.97}$	42.80	–	0.85	0.17	–
201	J033239.1-274440	1.80	$2.17^{+1.03}_{-0.83}$	42.49	–	0.679	0.15	–
202	J033229.9-275106	1.80	$36.85^{+20.54}_{-15.70}$	44.12	HEX	3.700	0.12	–
205	J033217.2-274137	1.80	$13.52^{+10.50}_{-6.52}$	43.06	–	1.56	0.08	–
210	J033238.4-275554	1.80	$1.72^{+4.72}_{-1.72}$	42.95	–	1.73	0.05	–
218	J033216.5-275200	1.80	<0.09	41.49	–	0.497	0.03	–
222	J033254.6-274501	1.80	$0.30^{+0.68}_{-0.30}$	42.97	–	1.14	0.13	–
226	J033204.5-274644	1.80	$0.11^{+1.40}_{-0.11}$	43.07	–	1.45	0.09	–
227	J033205.4-274644	1.80	$65.42^{+22.09}_{-16.52}$	43.94	–	2.18	0.26	–
230	J033153.6-274844	1.80	$1.30^{+4.54}_{-1.30}$	43.27	BLAGN	2.185	0.06	–
236	J033211.5-275006	1.80	<0.18	41.94	–	0.76	0.03	–
239	J033236.2-275127	1.80	$0.44^{+3.84}_{-0.44}$	42.55	–	1.47	0.03	–
240	J033259.2-275140	1.80	$3.70^{+3.70}_{-2.78}$	42.84	–	1.41	0.06	–
241	J033224.3-274258	1.80	$0.33^{+1.26}_{-0.33}$	41.96	–	0.70	0.04	–
247	J033234.9-275535	1.80	$0.27^{+0.80}_{-0.27}$	39.16	LEX	0.04	0.04	–
248	J033210.3-275418	1.80	$8.64^{+9.56}_{-4.54}$	42.19	ABS	0.685	0.07	–
249	J033219.5-275406	1.80	<0.12	42.31	–	0.96	0.04	–
251	J033207.2-275229	1.80	$27.56^{+25.30}_{-14.60}$	43.42	–	2.13	0.08	–
252	J033247.1-274346	1.80	$16.09^{+7.65}_{-5.68}$	43.05	LEX	1.180	0.14	–
253	J033220.1-274448	1.80	$10.77^{+4.24}_{-2.85}$	42.34	LEX	0.484	0.23	–
254	J033219.9-274519	1.80	$6.37^{+4.21}_{-2.24}$	40.63	Galaxy	0.10	0.15	–
256	J033243.1-274845	1.80	$33.70^{+16.03}_{-11.47}$	43.33	–	1.53	0.15	–
257	J033213.5-274857	1.80	$13.45^{+16.10}_{-7.47}$	42.13	–	0.549	0.10	–
259	J033206.2-274928	1.80	$46.86^{+13.56}_{-11.05}$	43.69	–	1.76	0.24	–
260	J033225.2-275044	1.80	54.90	41.78	LEX	1.043	0.01	–
261	J033157.1-275110	1.80	$2.04^{+0.66}_{-0.53}$	–	–	–	0.19	–
263	J033218.9-275136	1.80	$61.41^{+169.47}_{-54.33}$	43.69	–	3.660	0.05	–
264	J033229.8-275146	1.80	$27.72^{+17.49}_{-10.70}$	43.09	LEX	1.318	0.12	–
265	J033233.4-274236	1.80	$16.06^{+4.55}_{-3.89}$	43.34	–	1.22	0.25	–
266	J033214.0-274249	1.80	$38.89^{+24.49}_{-16.11}$	42.54	LEX	0.735	0.14	–
505*	J033305.0-274732	1.80	130^{+122}_{-63}	43.61	–	2.26	0.11	–
507	J033300.1-274925	1.80	$3.53^{+8.18}_{-3.47}$	42.39	–	0.99	0.05	–
508	J033251.8-275214	1.80	$57.52^{+47.57}_{-27.38}$	43.58	–	2.50	0.08	–
510	J033238.8-275122	1.80	$43.75^{+92.51}_{-32.60}$	43.34	–	2.51	0.05	–
511	J033236.6-274631	1.80	<1.41	41.68	–	0.767	0.02	–
512	J033234.5-274351	1.80	<0.82	41.72	LEX	0.665	0.03	–
513	J033234.1-274900	1.80	<12.82	43.31	–	3.56	0.02	–
514	J033233.6-274312	1.80	<0.42	39.85	ABS	0.10	0.02	–
515	J033232.2-274652	1.80	$50.29^{+41.21}_{-23.98}$	43.51	–	2.28	0.09	–
516	J033231.4-274727	1.80	$1.13^{+2.18}_{-1.13}$	41.92	LEX	0.665	0.04	–
518	J033226.9-274605	1.80	$2.47^{+4.33}_{-2.11}$	42.10	–	0.84	0.04	–
519	J033225.9-275508	1.80	<1.96	42.23	LEX	1.034	0.03	–
521	J033222.8-275225	1.80	$0.15^{+0.39}_{-0.15}$	40.34	LEX	0.131	0.04	–
522	J033221.5-275550	1.80	$2.04^{+6.12}_{-2.04}$	43.46	–	2.57	0.06	–
523	J033220.4-274229	1.80	$10.70^{+9.21}_{-6.32}$	42.70	–	1.32	0.05	–
524	J033220.0-274243	1.80	$16.13^{+12.66}_{-9.93}$	43.40	–	2.36	0.06	–
525	J033219.9-274123	1.80	$0.23^{+0.54}_{-0.23}$	40.84	LEX	0.229	0.04	–
526	J033218.8-274413	1.80	$8.51^{+16.30}_{-8.51}$	42.18	–	0.96	0.03	–
527	J033218.6-275414	1.80	$7.29^{+26.44}_{-7.29}$	43.87	–	4.49	0.04	–
528	J033217.1-275402	1.80	<0.32	42.30	–	1.43	0.02	–
529	J033216.3-275525	1.80	$4.02^{+5.04}_{-4.02}$	42.10	–	0.73	0.05	–
531*	J033214.5-275111	$-0.96^{+1.08}_{-2.04}$	<3.2	42.49	HEX	1.544	0.02	–

Table 3. continued.

ID	Name[1]	Γ[2]	$N_{\rm H}$[3]	$L_{\rm x}$[4]	Class[5]	z[6]	flux[7]	χ^2/d.o.f.
532	J033214.2-274231	1.80	$0.18^{+1.82}_{-0.18}$	42.12	–	0.95	0.03	–
534	J033212.2-274530	1.80	$13.09^{+10.40}_{-4.98}$	42.46	LEX	0.676	0.14	–
535*	J033211.5-274650	$0.59^{+0.52}_{-0.50}$	<0.29	42.12	LEX	0.575	0.09	–
536	J033210.9-274235	1.80	$0.79^{+1.72}_{-0.79}$	41.40	–	0.42	0.04	–
537	J033209.9-275016	1.80	$3.90^{+8.04}_{-3.90}$	42.68	–	1.54	0.03	–
538*	J033208.6-274649	$-1.1^{+1.7}_{-1.0}$	<1.0	41.62	LEX	0.310	0.12	–
540	J033202.7-275053	1.80	$3.52^{+13.12}_{-3.52}$	42.33	–	1.25	0.02	–
541	J033159.7-274949	1.80	$7.18^{+7.49}_{-5.15}$	43.07	–	1.82	0.05	–
543	J033157.0-275102	1.80	$3.55^{+12.21}_{-3.55}$	42.87	–	1.81	0.03	–
544	J033154.6-275104	1.80	$20.35^{+15.64}_{-10.92}$	43.42	–	2.36	0.07	–
597	J033251.4-275544	1.80	$25.01^{+69.25}_{-23.32}$	43.01	–	2.32	0.03	–
598	J033224.7-275413	1.80	$4.13^{+11.67}_{-4.13}$	41.71	ABS	0.617	0.03	–
599*	J033229.9-275329	1.80	100.0^{+65}_{-48}	43.58	–	2.84	0.06	–
600*	J033213.9-274526	1.80	380.0^{+180}_{-180}	44.43	LEX	1.33	0.26	–
602	J033222.0-274657	1.80	$97.81^{+106.02}_{-58.69}$	42.24	ABS	0.668	0.08	–
603	J033257.8-274711	1.80	$23.80^{+54.07}_{-23.80}$	42.82	–	2.04	0.02	–
605*	J033239.2-274833	1.80	2700^{+3800}_{-1700}	44.95	–	4.29	0.12	–
606	J033225.0-275009	1.80	$20.11^{+17.79}_{-9.79}$	42.68	–	1.037	0.08	–
607	J033159.7-275020	1.80	$16.32^{+14.49}_{-6.99}$	42.46	–	0.74	0.11	–
609*	J033236.2-275037	1.80	250^{+400}_{-170}	43.12	–	1.86	0.06	–
610*	J033219.9-275159	1.80	520^{+580}_{-280}	44.18	–	2.04	0.10	–
611	J033241.7-274328	1.80	$30.99^{+32.82}_{-14.91}$	42.64	-	0.979	0.09	–
612	J033221.4-274231	1.80	$35.72^{+26.07}_{-13.50}$	42.93	–	1.10	0.13	–
615	J033201.3-275052	1.80	$10.42^{+25.32}_{-10.42}$	42.03	LEX	0.759	0.04	–
632	J033233.5-275228	1.80	$33.91^{+60.75}_{-23.67}$	42.91	–	1.57	0.05	–
634*	J033251.5-274746	1.80	460^{+1500}_{-460}	42.72	–	1.40	0.05	–
635	J033216.9-275009	1.80	$1.50^{+3.55}_{-1.50}$	41.72	–	0.729	0.02	–
637	J033225.7-274332	1.80	$33.64^{+208.04}_{-31.62}$	42.12	–	0.76	0.05	–
638	J033230.0-274302	1.80	$4.83^{+407.27}_{-4.83}$	42.40	–	1.39	0.02	–
642*	J033215.3-274159	1.80	$130^{+\infty}_{-110}$	43.32	HEX	2.402	0.05	–

[1] Source name from Giacconni et al. (2002). [2] Best fit model power-law photon index. [3] Rest-frame column density in units of 10^{22} (cm^{-2}). [4] logarithm of 2–10 keV intrinsic luminosity (erg s^{-1}). [5] Optical spectroscopic classification as given in Szokoly et al. (2004). [6] Redshift from either Szokoly et al. (2004) (spectroscopic) or Zheng et al. 2004 (photometric). [7] observed 2–10 keV X-ray flux in units of 10^{-14} erg cm^{-2} s^{-1}. [9] Reduced χ^2. * Compton-thick sources.